Dynamics of the antiferromagnetic spin ice phase in pyrochlore spinels

Attila Szabó[1,2,3] and Gøran J. Nilsen[1,4]

[1]*ISIS Facility, Rutherford Appleton Laboratory, Harwell Campus, Didcot OX11 0QX, United Kingdom*
[2]*Rudolf Peierls Centre for Theoretical Physics, University of Oxford, Oxford OX1 3PU, United Kingdom*
[3]*Max Planck Institute for the Physics of Complex Systems, Nöthnitzer Str. 38, 01187 Dresden, Germany*
[4]*Department of Mathematics and Physics, University of Stavanger, 4036 Stavanger, Norway*

(Received 31 May 2023; revised 5 January 2024; accepted 17 January 2024; published 21 March 2024)

Motivated by the classical spin-nematic state observed in the breathing pyrochlore spinel $LiGa_{0.95}In_{0.05}Cr_4O_8$, we theoretically discuss spin dynamics in models of spin-lattice coupling in these materials. Semiclassical dynamical simulations successfully recover the key features of inelastic neutron-scattering experiments on $LiGa_{0.95}In_{0.05}Cr_4O_8$: a broad finite-energy peak alongside a continuum of scattering near the (200) wave vector that extends from the elastic line to high energies. To interpret this result, we generalize linear-spin-wave theory for conventionally ordered magnets to the disordered spin-ice-like ground states expected for moderate spin-lattice coupling, which reproduces the numerical simulation results quantitatively. In particular, we find that the inelastic peak is well explained by collective modes confined to ferromagnetic loops of the underlying nematic order. In addition, we find a sharp, linearly dispersing mode in the dynamic structure factor, which originates in long-wavelength fluctuations of the nematic director. We believe identifying this mode will be an interesting target for future experiments on these materials. We also outline potential future applications of our methods to both pyrochlore spinels and other spin-nematic systems.

DOI: 10.1103/PhysRevB.109.104425

I. INTRODUCTION

Frustrated magnets are characterized by competing magnetic interactions that cannot be satisfied by any single classical ground state. Theoretical models of such systems exhibit a variety of exotic phases, including spin liquids characterized by extensive ground-state degeneracy, fractional excitations, and topological order [1–3]. In real magnetic materials, however, such spin-liquid behavior is usually suppressed by additional (e.g., further-neighbor or spin-lattice) interactions and disorder, yielding conventional order or a spin glass [4].

Spinel pyrochlores of formula AB_2O_4, where the magnetic B ions form a lattice of corner-sharing tetrahedra, exhibit a variety of such mechanisms. For example, the magneto-structural order of $ZnCr_2O_4$ at low temperature involves both a lowering of symmetry from cubic to tetragonal and a doubling of the unit cell, as well as a noncollinear spin arrangement [5]. This complexity arises from the interplay between further-neighbor interactions and spin-lattice coupling [6–8]. In the $Zn_{2-x}Cd_xCr_2O_4$ solid solution, on the other hand, the introduction of bond disorder by chemical substitution produces an apparent spin glass ground state for even small values of x [9].

Perhaps the most intriguing mechanism for relieving frustration in spinels is the spin–lattice coupling due to the rich phase diagrams and novel states it generates [5–7,10–14]. The simplest approach to model this interaction is to consider a bond-length-dependent Heisenberg model coupled to phonons that modulate the bond lengths independently. Integrating out the phonons then results in the bilinear-biquadratic (BLBQ) effective Hamiltonian [6,10,15]

$$\mathcal{H} = \sum_{\langle ij \rangle} [J\vec{s}_i \cdot \vec{s}_j - Q(\vec{s}_i \cdot \vec{s}_j)^2]. \tag{1}$$

In the large-S limit (a justified approximation for the $S = 3/2$ Cr^{3+} ions), the pure Heisenberg model $Q = 0$ is a classical spin liquid [16]. Spin–lattice coupling introduces a finite $Q > 0$, which causes the model to develop collinear nematic order at $T \simeq Q$ [11]. This order, however, retains residual frustration. Once all spins align along a nematic director to optimize the Q term, the J term becomes equivalent to nearest-neighbor spin ice, which is optimized by exponentially many two-up-two-down states [17]. While the BLBQ model has been very successful in describing the magnetization plateaux of several pyrochlore spinels [10,12,18–20], longer-range interactions not captured by (1) cause most of them to exhibit full magnetic ordering rather than the predicted nematic spin-ice state. In particular, the BLBQ model decouples the length modulation of different bonds around the same site: in the more realistic *site-phonon model* [13,21], phonons mediate further-neighbor multi-spin couplings that explain such orders as the plateau phases of $CdCr_2O_4$ and $HgCr_2O_4$ [20].

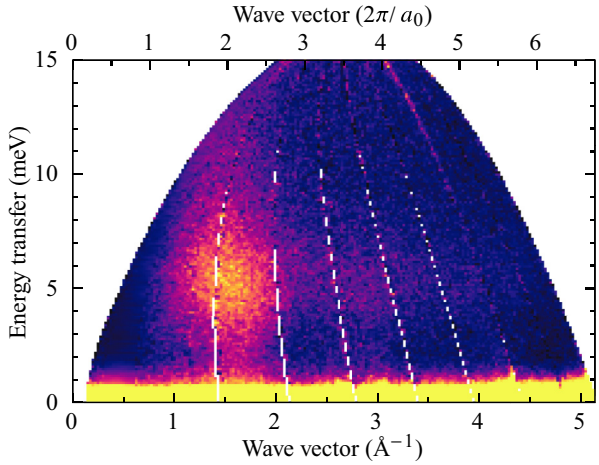

FIG. 1. Powder-averaged inelastic-neutron-scattering intensity of $LiGa_{0.95}In_{0.05}Cr_4O_8$ measured at $T = 5.2$ K using 16 meV incident neutron energy [25]. The neutron-scattering pattern is dominated by a peak at finite energy transfer near the (200) reciprocal lattice vector (the cubic lattice constant of $LiGa_{0.95}In_{0.05}Cr_4O_8$ is $a_0 = 8.253$ Å [26]).

In the past decade, much of the attention on pyrochlore spinels has shifted to the breathing pyrochlores $AA'Cr_4O_8$, where the ordering of the A and A' cations cause translation-inequivalent (up- and down-pointing) tetrahedra in the pyrochlore lattice to have different sizes and hence exchange couplings. High-temperature susceptibility measurements on the two best-known materials in the family, $LiGaCr_4O_8$ and $LiInCr_4O_8$, indicate a ratio of Heisenberg couplings J'/J of around 0.6 and 0.1 between the inequivalent tetrahedra, respectively [22]. At low temperatures, both materials show magneto-structural ordering driven by spin–lattice coupling [21,23,24], alongside phase separation due to site disorder.

Mixing Ga and In on the A' site, however, quickly suppresses this ordering, with a possible gapped spin liquid on the In-rich side of the phase diagram, and a spin glass on the Ga-rich side [26]. For $LiGa_{0.95}In_{0.05}Cr_4O_8$ (with J'/J close to that of $LiGaCr_4O_8$), neutron-diffraction and specific-heat measurements indicate that the nematic state predicted by the BLBQ model (1) is stabilized [14]. This implies that the bond disorder introduced by the Ga–In mixing is weaker than the leading biquadratic interaction generated by spin–lattice coupling, allowing nematic ordering, but it is strong enough to disrupt full ordering, stabilising instead a glassy spin-ice state [11], similar to dipolar spin ice [27]. Inelastic-neutron-scattering experiments on $LiGa_{0.95}In_{0.05}Cr_4O_8$ [25] (Fig. 1) found a broad peak in the dynamical structure factor $\mathcal{S}(q,\omega)$ at $\hbar\omega \approx 5.5$ meV and wave vector $q \approx 1.6$ Å^{-1} (corresponding approximately to the (200) reciprocal lattice vector for the cubic lattice constant $a_0 = 8.253$ Å [26]), tentatively ascribed to excitations localized on antiferromagnetic hexagon loops.

In this paper, we explore the dynamics of $LiGa_{0.95}In_{0.05}Cr_4O_8$ and the nematic state of breathing pyrochlores in general. Our main focus will be the classical BLBQ model, generalized to the breathing lattice:

$$\mathcal{H} = \sum_{\langle ij\rangle\in\uparrow} [J\vec{s}_i\cdot\vec{s}_j - Q(\vec{s}_i\cdot\vec{s}_j)^2] + \sum_{\langle ij\rangle\in\downarrow} [J'\vec{s}_i\cdot\vec{s}_j - Q'(\vec{s}_i\cdot\vec{s}_j)^2], \tag{2}$$

where $\uparrow$ and $\downarrow$ stand for the translation-inequivalent up- and down-pointing tetrahedra of the pyrochlore lattice, respectively. For brevity, we will use units in which the spin magnitude $|\vec{s}_i|$ is 1 [28] and introduce $\overline{J} = (J + J')/2$, $\overline{Q} = (Q + Q')/2$.

In Sec. II, we discuss simulations of the semiclassical Landau–Lifshitz dynamics under (2); this semiclassical approximation is justified in the $|Q| \ll |J|$ limit, where the dominant Heisenberg coupling stabilizes a ground state with dipole, rather than quadrupole, moments [29–32]. The numerically obtained dynamical structure factor is dominated by a broad peak at $\hbar\omega = 16\overline{Q}$, a sharp linearly dispersing mode at small q, ω, and a weak continuum extending up to about $4\overline{J}$. We discuss the fate of these features in the presence of Landau-Lifshitz damping and structural disorder; in Sec. III, we explain them in terms of linear "spin-wave" theory around the disordered spin-ice ground states of (2). We find that the $16\overline{Q}$ peak is caused by out-of-phase precession around *ferromagnetic* loops of spins, while the linearly dispersing feature originates in long-wave fluctuations of the nematic director. We perform the same analysis for the more complex site-phonon model as well: we find that all qualitative features of the BLBQ dynamics survive; the additional interactions, however, induce strong effective disorder and renormalize the spin-lattice coupling parameter Q by a factor of two. We discuss our findings in the context of experimental results in Sec. IV.

II. DYNAMICAL SIMULATIONS

We drew initial configurations from the thermal ensemble $e^{-\beta\mathcal{H}}$ using single-spin-flip Metropolis Monte Carlo on $16\times16\times16$ pyrochlore cubic unit cells (65 536 spins). Similar to Ising spin ice [27], we expect Monte Carlo dynamics to slow down substantially in the nematic phase. Therefore, to avoid getting stuck in local minima that do not satisfy the ice rules, we used simulated annealing from a temperature well above the nematic transition [at least $2\max(Q, Q')$] down to $T = 0.01\overline{J}$, well below the transition in every case, where we performed all dynamical simulations.

We then computed the time evolution of the initial spin configurations under the stochastic Landau–Lifshitz dynamical equation

$$\hbar\frac{d\vec{s}_i}{dt} = \vec{s}_i\times(\vec{B}_i + \vec{b}_i) - \alpha\vec{s}_i\times\vec{s}_i\times(\vec{B}_i + \vec{b}_i), \tag{3}$$

where $\vec{B}_i = -\partial\mathcal{H}/\partial\vec{s}_i$ is the effective field acting on spin $\vec{s}_i$ and $\vec{b}_i$ is a stochastic field satisfying the fluctuation–dissipation relation [33]

$$\langle b_i^\alpha(t)\rangle = 0;$$
$$\langle b_i^\alpha(t)b_j^\beta(t')\rangle = 2D\delta_{ij}\delta^{\alpha\beta}\delta(t-t'),$$
$$D = \frac{\alpha}{1+\alpha^2}k_B T\hbar. \tag{4}$$

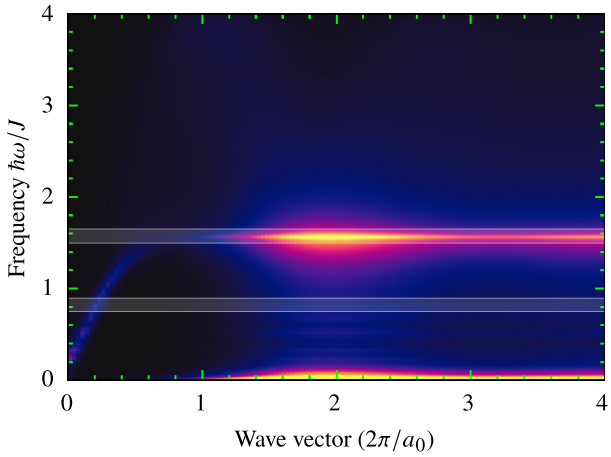

FIG. 2. Simulated powder-averaged dynamic structure factor for $J = J'$, $Q = Q' = 0.1J$, and $\alpha = 0.01$, using a cluster of 16^3 cubic unit cells. The pattern is dominated by a sharp maximum at $\hbar\omega \approx 1.6J$ and a linearly dispersing mode that connects this maximum to the origin. It also contains a broad continuum extending from the elastic line up to $\sim 4J$.

We note that the sign of the precession term in (3) is flipped compared to its usual presentation [34], as we take the negative gyromagnetic ratio of the electron into account through the definition of $\vec{B}_i$. Details of the numerical method are described in Appendix A; we benchmarked the simulations by ensuring that thermodynamic properties, such as the average energy, match the Monte Carlo results within statistical error.

We first focused on the case $J = J'$, $Q = Q' = 0.1J$, and $\alpha = 0.01$. The powder-averaged dynamical correlation function $S(q, \omega)$ is plotted in Fig. 2. Similar to the experimental powder neutron-scattering pattern of Ref. [25], we see a prominent scattering maximum at energy transfer $\hbar\omega \approx 1.6J$, with the highest intensity at $q \approx 4\pi/a_0$, where a_0 is the lattice parameter. In addition, we observe a linearly dispersing branch, extending from the origin to about the frequency of the intensity maximum.

We also plotted the static structure factor $S(q)$, as well as $S(q, \omega)$ integrated over two frequency windows, in Fig. 3. The static structure factor shows sharp pinch points in the pattern seen in Ref. [35] for spin ice; this is expected as the effective Ising spins in the nematic order obey the same ice rules. The same pinch points, albeit much broadened, are seen at finite ω as well. Below the intensity maximum at $1.6J$, we also see sharp circular features, which correspond to the linearly dispersing mode in Fig. 2.

As shown in Fig. 4, these features of the scattering pattern are quite robust in parameter space. While the model with $J' = Q' = 0$ is qualitatively different from the symmetric case (it is made up of disconnected tetrahedra), most features of the latter are already recovered for $J/J' = 0.2$ and the powder patterns at $J'/J \geqslant 0.4$ only differ in quantitative details. Likewise, the scattering pattern of the pure Heisenberg model $Q = Q' = 0$ is qualitatively different due to the lack of nematic ordering, but any finite Q is enough to bring about both the linearly dispersing mode and a broad scattering maximum at $16\overline{Q}$.

The intensity maximum at $16\overline{Q}$ in our simulations is much sharper than the analogous experimental feature [25]. This may either be because interactions with other dynamical degrees of freedom (e.g., magnon-magnon interactions) induce stronger damping than the Landau–Lifshitz damping term $\alpha = 0.01$ used above, or because the exchange couplings J, Q are disordered due to structural disorder or magnetoelastic distortions [11]. To distinguish these possibilities, we performed dynamical simulations at $J = J'$, $Q = Q' = 0.1J$ for two additional values of $\alpha = 0.1$ and 0.001, as well as the disordered model

$$\mathcal{H} = \sum_{\langle ij \rangle} [J_{ij} \vec{s}_i \cdot \vec{s}_j - Q_{ij} (\vec{s}_i \cdot \vec{s}_j)^2], \tag{5}$$

where J_{ij} (Q_{ij}) are drawn independently from a Gaussian distribution with mean J (Q) and standard deviation $0.1J$ ($0.1Q$). The results are summarized in Fig. 5. The $16\overline{Q}$ feature is broadened by a similar amount both for $\alpha = 0.1$ [Fig. 5(a)] and on introducing disorder [Fig. 5(b)]. The line shapes of the q-integrated structure factor [Fig. 5(c)] appear Lorentzian and Gaussian, respectively, although they are difficult to distinguish due to the background intensity. The linearly dispersing

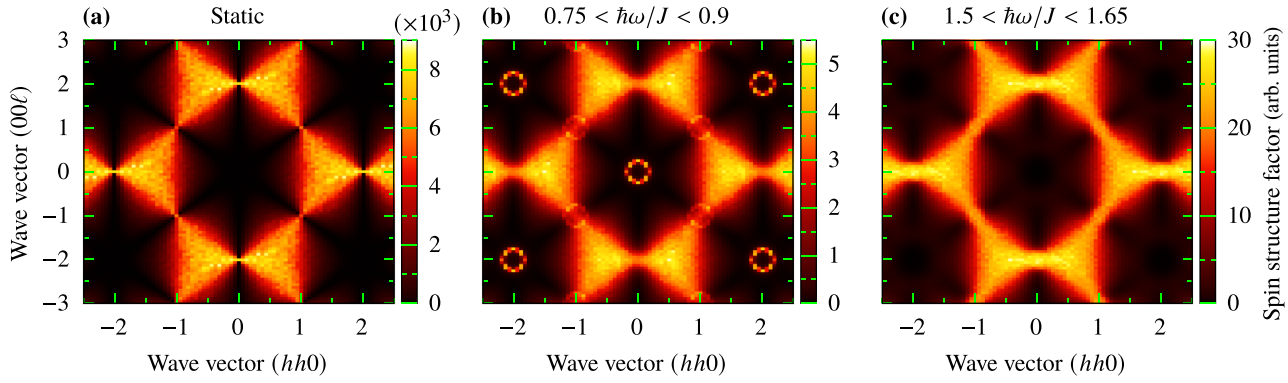

FIG. 3. Static and frequency-window-integrated dynamic structure factors in the $(hh\ell)$ plane for the same parameters as in Fig. 2. All three panels show pinch points, consistent with the spin-ice-like nematic ground state; in addition, the linearly dispersing mode seen in Fig. 2 appears as sharp circular features in (b). The frequency windows used in (b) and (c) are highlighted with lighter background in Fig. 2. The "arbitrary units" are consistent across the three plots: the static structure factor, dominated by the $\omega = 0$ component, is much larger than dynamical correlations, consistent with (nematic) ordering.

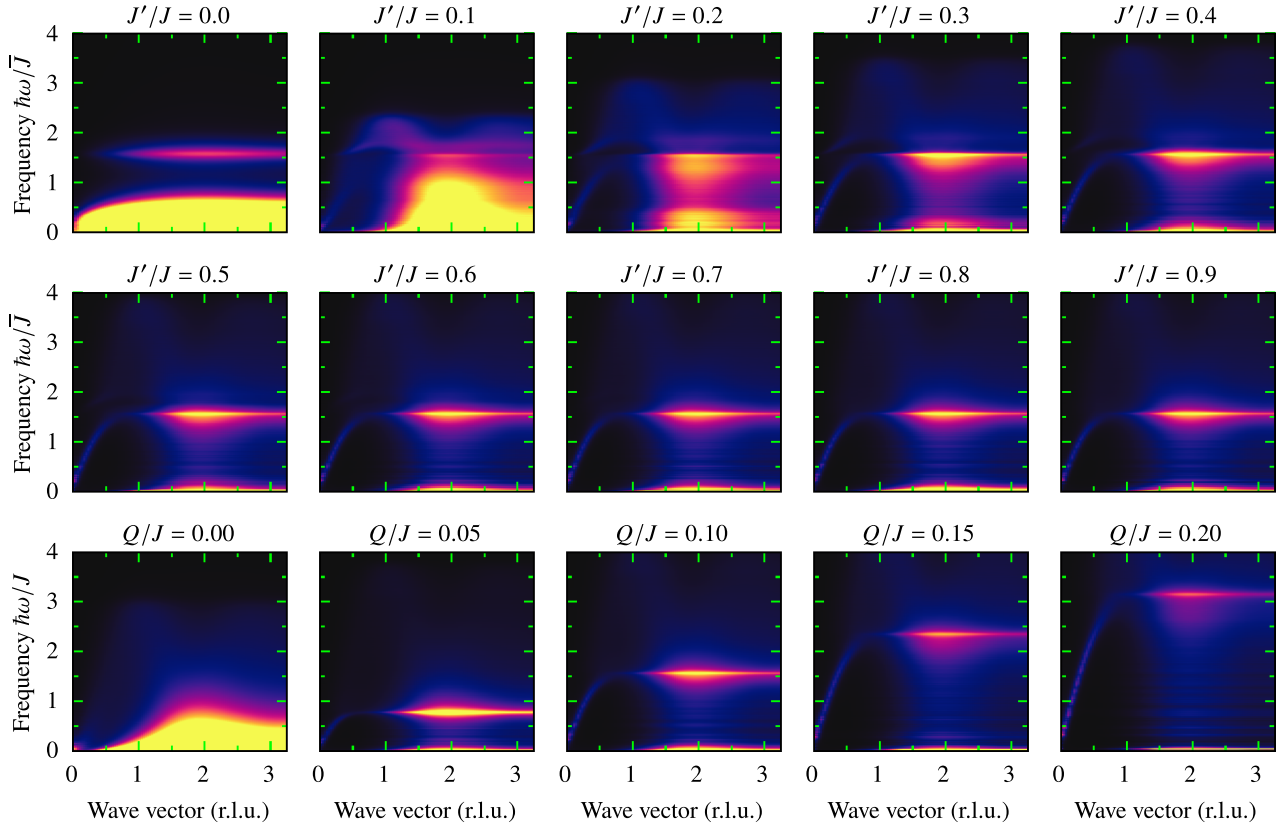

FIG. 4. Simulated powder-averaged dynamic structure factor for several J'/J at $Q/J = Q'/J' = 0.1$ (top two rows) and for several Q/J at $J = J'$ and $Q = Q'$ (bottom row). Except for $J' \ll J$ and $Q = 0$, where the nematic ordering breaks down, the pattern is dominated by a broad feature at $16\overline{Q}$ and a linearly dispersing mode stretching from the origin to this feature. The colors indicate the same range of intensities in all panels except the last four; these are scaled as $I_{\max} \propto 1/Q$ to keep the total intensity of the $16Q$ feature visually constant. All simulations use a cluster of 16^3 cubic unit cells.

mode, however, behaves qualitatively differently: it does not blur noticeably on introducing disorder but becomes broad and faint beyond the point of clear detection on increasing α [see also Fig. 5(d)]. Lowering α causes the low-frequency structure factor to decompose into discrete normal modes of the finite simulation box, resulting in an array of sharp peaks in Fig. 5(c).

Finally, we considered dynamics under the site-phonon Hamiltonian

$$\mathcal{H}_{\text{sp}} = \sum_{\langle ij\rangle\in\uparrow} J\vec{s}_i\cdot\vec{s}_j + \sum_{\langle ij\rangle\in\downarrow} J'\vec{s}_i\cdot\vec{s}_j - \frac{1}{2}\sum_i\sum_{j,k\sim i}\sqrt{Q_{ij}Q_{ik}}(\hat{e}_{ij}\cdot\hat{e}_{ik})(\vec{s}_i\cdot\vec{s}_j)(\vec{s}_i\cdot\vec{s}_k), \quad (6)$$

where the inner sum runs over all pairs j, k of nearest neighbors of site i (j, k and k, j are both counted), $Q_{ij} = Q$ (Q') if the bond ij is part of an up (down) tetrahedron, and $\hat{e}_{ij}$ is the unit vector pointing from site i to j. Since this Hamiltonian has a fully ordered ground state [13,21], we emulated the glassy nematic order of $LiGa_{0.95}In_{0.05}Cr_4O_8$ by first preparing low-temperature states of the BLBQ Hamiltonian and annealing them under (6) before measuring dynamical correlation functions. At $J = J', Q = Q' = 0.1J$, we obtained the powder-averaged structure factors shown in Fig. 6; see Appendix A 4 for a wider range of parameters. The general structure of the powder pattern remains unchanged and, in particular, the nematic state appears to be metastable even without quenched disorder. However, the finite-frequency peak becomes much broader, and the peak frequency is reduced substantially, from $16Q$ to about $7Q$. The linearly dispersing mode remains sharp, but its velocity is reduced, too.

Remarkably, we see a strong modulation of the intensity with frequency that appears to split the peak into a number of fringes. Similar, albeit weaker, fringes have already appeared in the BLBQ model [cf. Fig. 5(b)]: these are a finite-size effect caused by the gap between the discrete normal modes that make up the linearly dispersing branch in a finite simulation box. To rule out this origin for the modulation seen in the site-phonon model, we performed dynamical simulations on clusters of L^3 cubic unit cells for every $12 \leqslant L \leqslant 17$. After averaging the powder pattern for the different clusters, several fringes at low frequencies (where finite-size effects are the most pronounced) indeed disappear; however, the finite-frequency peak remains split into three (around $0.45J$, $0.6J$, and $1.1J$ in Fig. 6). Nevertheless, we expect that these fringes would be washed out by either stronger damping or quenched disorder, which is expected to cause similar peak broadening to that seen for the BLBQ model in Fig. 5.

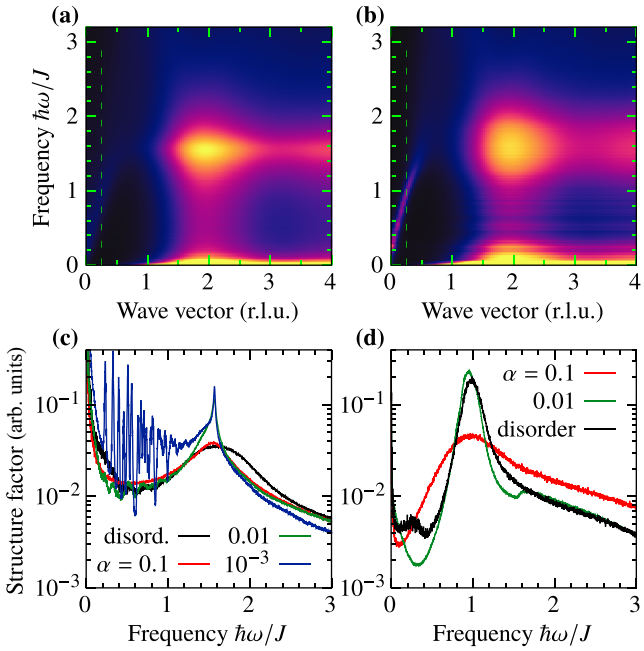

FIG. 5. [(a) and (b)] Simulated powder-averaged dynamic structure factor for the same parameters as Fig. 2 but with $\alpha = 0.1$ (a) or 10% Gaussian disorder in J and Q [Eq. (5), (b)]. (c) q-integrated structure factors for the disordered model and three values of α. (d) Cuts of the powder pattern for the disordered model and two values of α at $q = \pi/(2a_0)$ [dashed green lines in (a) and (b)]. The "arbitrary units" are not consistent between panels (c, d).

III. LINEAR SPIN-WAVE THEORY (LSWT)

To explain the salient features of the numerically obtained dynamical structure factor, we now construct a small-fluctuation theory, similar to linear spin-wave theory for ordered magnets, for the spin-ice-like nematic ground state. Namely, we observe that the low-temperature dynamics consists primarily of small transverse fluctuations around the equilibrium state, a spin-ice configuration with an arbitrary Ising axis (the nematic director). Without loss of generality,

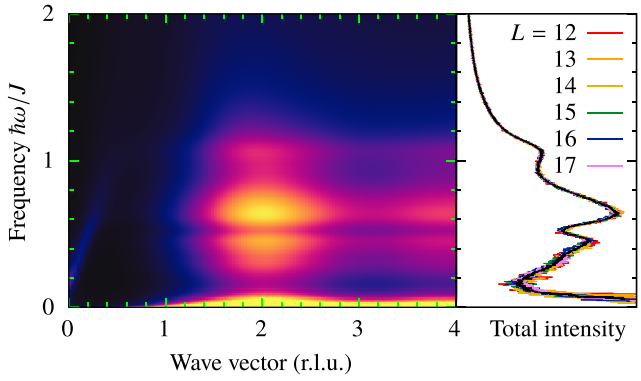

FIG. 6. Simulated powder-averaged (left) and q-integrated (right) dynamic structure factor for the same parameters as Fig. 2 in the site-phonon model (6). The powder pattern is averaged from simulations of clusters with L^3 ($L = 12, \ldots, 17$) cubic unit cells; the integrated structure factor is shown for each cluster as well as the average.

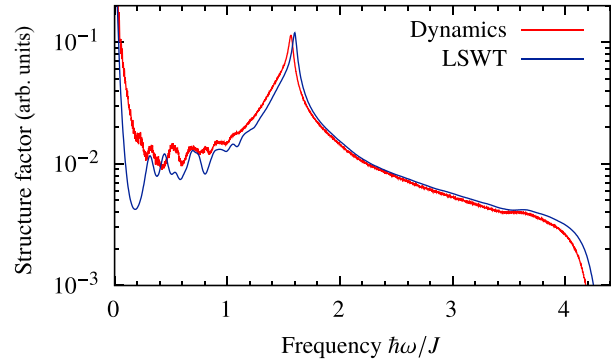

FIG. 7. q-integrated structure factor obtained from dynamical simulations (red) and linear spin-wave theory (blue) for $J = J'$, $Q = Q' = 0.1J$, $\alpha = 0.01$.

we choose this axis to be $\pm s^z$, so we can write

$$\vec{s}_i \simeq \left(\mathrm{Re}\, s_i^+, \mathrm{Im}\, s_i^+, Z_i\sqrt{1 - s_i^+ s_i^-}\right), \tag{7}$$

where the Ising variables $Z_i = \pm 1$ satisfy the ice rules, and $s_i^+ \sim \sqrt{T/\bar{J}} \ll 1$. Substituting this into (2) and expanding to quadratic order in $s^\pm$ gives

$$\mathcal{H} = \text{const.} + \frac{1}{2}\sum_{ij} s_i^- H_{ij} s_j^+, \tag{8}$$

where the nonzero matrix elements H_{ij} are

$$H_{ij} = \begin{cases} J + J' + 6(Q + Q') & i = j \\ J - 2QZ_iZ_j & \langle ij\rangle \in \uparrow \\ J' - 2Q'Z_iZ_j & \langle ij\rangle \in \downarrow \end{cases} \tag{9}$$

in an ice-like arrangement of Z_i. Likewise, substituting (7) into the dynamical equation (3) (without the stochastic fields $\vec{b}_i$) and expanding to linear order gives (see Appendix B)

$$\hbar\frac{ds_i^+}{dt} = -(iZ_i + \alpha)\sum_j H_{ij} s_j^+. \tag{10}$$

The dynamical modes of (10) and their frequencies are given by the eigenvalue equation

$$(Z - i\alpha)H|r_a\rangle = \hbar\omega_a|r_a\rangle, \tag{11}$$

where we introduce bra-ket notation for the vectors comprised of all s_i^+ and define for convenience the diagonal matrix Z with the Ising configuration Z_i along the diagonal. For $\alpha = 0$, all eigenfrequencies of (11) are real (see Appendix C), as expected for energy-conserving dynamics near a ground state. Likewise, for $\alpha > 0$, all modes decay exponentially.

We diagonalized (11) for a cluster of $12 \times 12 \times 12$ cubic unit cells (27 648 spins), for both $\alpha = 0$ and 0.01. As explained in Appendix D, these eigenvalues and eigenvectors can be used to compute the dynamical structure factor $S(q, \omega)$ within the linear-spin-wave approximation. We find excellent quantitative agreement in the q-integrated structure factor (Fig. 7) as well as the powder pattern (not shown). The two curves in Fig. 7 differ in two ways. First, the low-frequency oscillations show a different pattern due to the different system sizes (and thus different low-frequency modes). Second,

higher-frequency features of the LSWT spectrum are consistently shifted to slightly higher frequencies. This is due to spin-wave interactions, most of which can be accounted for in a simple mean-field picture: As the length $|\vec{s}_i|$ of spins is fixed to 1, transverse fluctuations cause $\langle|s_i^z|\rangle =: s_0$ to shorten, which renormalizes the coefficients of (10) as $J \mapsto Js_0$, $Q \mapsto Qs_0^3$ [25,28]. From (D6), we estimate $s_0 = \sqrt{1 - \langle s_i^+ s_i^-\rangle} \approx 0.9916$; scaling LSWT frequencies by a factor of s_0^3 indeed causes the $16Q$ peaks of the two curves to overlap perfectly.

In summary, spin waves give a full, quantitative account of the inelastic spin dynamics, and nonlinear effects affect the spin-wave spectrum only weakly at low temperatures. In the following sections therefore, we will explain the salient features of the dynamical structure factor in terms of particular eigenmodes of the dynamical equation (10).

A. Exact eigenmodes at $16\overline{Q}$

In the spectrum of ZH, we see an accumulation of eigenvalues near $16\overline{Q}$. More interestingly, a number (140 for the pattern of Z_i we used) of eigenfrequencies are equal to $\pm 16\overline{Q}$ *within numerical accuracy* for $\alpha = 0$. We also observe that these exact eigenmodes live exclusively on up spins (for $\omega > 0$) or down spins (for $\omega < 0$).

Since the (real-space) LSWT matrix H only has on-site and nearest-neighbor matrix elements, we can decompose it into terms acting on a single tetrahedron only. These terms have the form

$$H_\uparrow = \begin{pmatrix} J+6Q & J-2Q & J+2Q & J+2Q \\ J-2Q & J+6Q & J+2Q & J+2Q \\ J+2Q & J+2Q & J+6Q & J-2Q \\ J+2Q & J+2Q & J-2Q & J+6Q \end{pmatrix}, \quad (12)$$

on each up tetrahedron; for down tetrahedra, $J \to J', Q \to Q'$. The first two and last two rows and columns of the matrix correspond to the two up ($Z = +1$) and two down ($Z = -1$) spins, respectively. $H_\uparrow$ has two eigenvectors with eigenvalue $8Q$: they are orthogonal to both (1,1,1,1) (i.e., they respect the ice rules) and the vector of Ising spin components (Z_1, Z_2, Z_3, Z_4) on the tetrahedron. By enforcing these constraints on every tetrahedron, we can construct a number of eigenmodes of H; the corresponding eigenvalue is $8(Q + Q') = 16\overline{Q}$ as every spin belongs to one up and one down tetrahedron.

To obtain an eigenvector of the dynamical matrix ZH from this construction, we need them to be eigenvectors of Z as well, so they must be constrained to up ($Z = +1$) or down ($Z = -1$) spins in the nematic Ising configuration. On each tetrahedron, there are two configurations that obey all of these requirements: out-of-phase fluctuations of either the two up or the two down spins. We can build joint eigenstates of H and Z from these by following closed loops of up or down spins and giving nearest neighbors out-of-phase fluctuations. In periodic boundary conditions, the loops always close and are of even length, so the resulting fluctuation vectors are exact eigenvectors of both H and the dynamical matrix ZH. Therefore, they are also eigenmodes of the damped dynamics (11) with complex frequency $\hbar\omega = 16(\pm 1 - i\alpha)\overline{Q}$, as we also found in exact diagonalization.

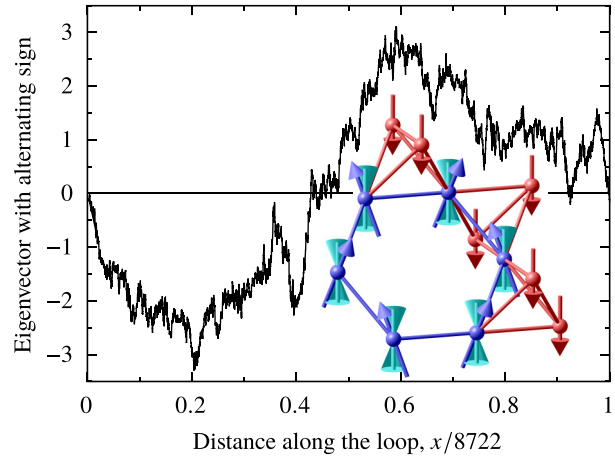

FIG. 8. An eigenvector $|r\rangle$ of the $\alpha = 0$ dynamical matrix with frequency $\hbar\omega/J = -1.6 + 3.01 \times 10^{-8}$ (the closest to $\pm 16Q$ that is not equal to it), restricted onto the longest closed loop of down spins, where 93% of its statistical weight falls. (Inset) Illustration of the exact $16\overline{Q}$ eigenmode on the shortest possible ferromagnetic loop (blue atoms). Magnetic moments around the loop (blue arrows) precess around their equilibrium Ising direction (cones); the fluctuations of nearest neighbors are out of phase.

These ferromagnetic loops are uniquely defined, since each spin has two neighbors with the same value of Z (one on each tetrahedron it belongs to). By constructing them on simulated ice configurations, we found that their lengths have a very broad distribution: a few loops cover almost all spins, while the remaining spins form very small loops, often as small as a single hexagon. The exact eigenmodes on the latter resemble the "weathervane modes" proposed in Ref. [25] (inset of Fig. 8).

The exact eigenmodes described above, however, do not account for the full intensity of the $16\overline{Q}$ peak in the dynamical structure factor, or the high density of LSWT eigenmodes *near* this frequency. On a long loop, however, we can consider "excited loop states," in which the exact eigenmode with alternating phases is modulated with a standing wave along the loop. Locally, this pattern is very similar to the exact eigenmode, and we therefore expect such states to be eigenmodes to a good approximation, with frequencies very close to $\pm 16\overline{Q}$. A few numerically obtained eigenmodes of ZH follow this pattern closely (Fig. 8) and most of those near $\omega = \pm 16\overline{Q}$ show similar features, albeit obscured somewhat by local interference between different loops. Furthermore, the fact that these modes live on loops explains the singular cusp, characteristic of *one-dimensional* van Hove singularities, in the structure factor.

B. Low-frequency dispersive modes

For $\alpha = 0$, we found that the lowest-magnitude eigenvalues of both H and the dynamical matrix ZH organize themselves in approximate multiplets (Fig. 9). Their multiplicities match those of the reciprocal lattice vectors $\{100\}, \{110\}, \{111\}, \{200\}, \ldots$ of the cubic simulation box, while the eigenvalues of ZH and H scale with the same wave vectors as $\omega \propto \pm|k|$, $\varepsilon \propto k^2$, respectively. This indicates a

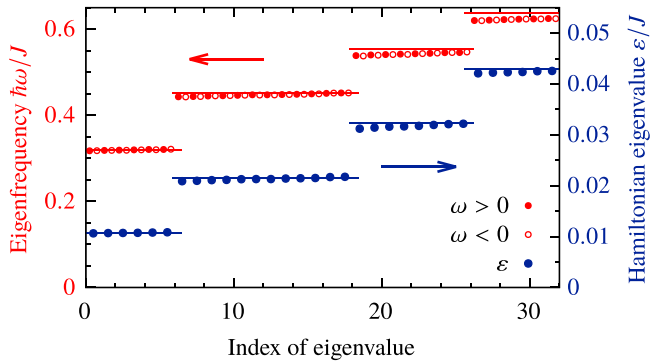

FIG. 9. Lowest-magnitude eigenvalues of H (blue) and ZH (red). The spectrum forms approximate multiplets of multiplicity 6, 12, 8, 6, … (one sequence each for $\pm\omega$). The eigenvalues in the nth multiplet scale as $\omega \propto \pm\sqrt{n}$ and $\varepsilon \propto n$ (indicated by the horizontal lines) to a good approximation.

linearly dispersing dynamical mode, consistent with the dynamical simulations. The corresponding eigenvectors do not show a particularly high overlap with the plane waves $|k\rangle$, but rather with the vectors

$$Z|k\rangle = \sum_i Z_i e^{i\vec{k}\cdot\vec{r}_i}|\text{site } i\rangle. \tag{13}$$

At $k = 0$, this mode corresponds to rotating the Ising axis of the nematic order; for small k, it captures long-wavelength fluctuations of the director, which we anticipate to cost little energy.

To explain these findings, we first note that both $|k\rangle$ and $Z|k\rangle$ are approximate eigenmodes of H for small k. The first closely resembles the all-in-all-out configuration (1,1,1,1) on each tetrahedron, which is an eigenvector of the single-tetrahedron Hamiltonian (12) with eigenvalue $4J + 8Q$. Since each spin belongs to one up and one down tetrahedron, these contributions add up to give

$$H|k\rangle = \underbrace{[4(J + J') + 8(Q + Q')]}_{E}|k\rangle + O(k^2). \tag{14}$$

In the limit $J \to 0$, $Z|k\rangle$ is an *exact* eigenvector of H with eigenvalue $\varepsilon(k) = \overline{Q}k^2/4 + O(k^4)$, since the matrix ZHZ is translation invariant in this limit [36]. A finite J adds disordered terms to ZHZ that penalize fluctuations proportional to the Ising configuration Z_i on each tetrahedron. However, the weight of such fluctuations is only $O(k^2)$ as the plane wave $|k\rangle$ is proportional to $(1, 1, 1, 1) + O(k)$ on each tetrahedron. That is, even if $J \gg Q$ causes these fluctuations to be completely projected out, the resulting eigenmode of ZHZ is still $|k\rangle$ up to $O(k^2)$ corrections. That is,

$$\begin{aligned} ZHZ|k\rangle &= \varepsilon(k)[|k\rangle + O(k^2)], \\ H(Z|k\rangle) &= \varepsilon(k)[Z|k\rangle + O(k^2)], \end{aligned} \tag{15}$$

where $\varepsilon(k) \propto k^2$.

Now, up to $O(k^2)$ corrections, the dynamical equation (11) can be written for a mode $|r\rangle = aZ|k\rangle + b|k\rangle$ as

$$\hbar\omega\begin{pmatrix} a \\ b \end{pmatrix} = \begin{pmatrix} -i\alpha\varepsilon(k) & E \\ \varepsilon(k) & -i\alpha E \end{pmatrix}\begin{pmatrix} a \\ b \end{pmatrix}. \tag{16}$$

For $\alpha = 0$, we obtain the eigenmodes

$$\hbar\omega = \pm\sqrt{\varepsilon(k)E}, \tag{17a}$$

$$|r\rangle = Z|k\rangle \pm \sqrt{\varepsilon(k)/E}\,|k\rangle. \tag{17b}$$

The numerically obtained ε and ω plotted in Fig. 9 match (17a) closely. Since $\varepsilon(k) \ll E$, the modes (17b) are dominated by $Z|k\rangle$, but the small admixture of $|k\rangle$ is enough to yield a visible dispersing mode, as it is not diffuse in k space.

For $\alpha \neq 0$, the complex eigenfrequencies of (16) are

$$\hbar\omega = -i\alpha\frac{\varepsilon(k) + E}{2} \pm \sqrt{\varepsilon(k)E - \alpha^2\left(\frac{\varepsilon(k) - E}{2}\right)^2}. \tag{18}$$

Even for small α, the decay rate $\operatorname{Im}\omega$ is independent of k, thus coherent oscillations at the longest wavelengths are always disrupted (the square root in (18) becomes imaginary, indicating purely decaying modes). For $\alpha = 0.1$, this becomes the case for most values of k, that is, the linearly dispersing modes blur completely, as seen in the dynamical simulations. By contrast, we expect that they remain robust against disorder: since they are dominated by long-wave modulations of the nematic director, they are only sensitive to coarse-grained averages of the exchange couplings J, Q, which are affected far less by disorder.

C. Site-phonon model

Finally, we consider the site-phonon Hamiltonian (6). Expanding the Hamiltonian to quadratic order is somewhat more complicated than in the BLBQ case and is described in detail in Appendix E. We find that, despite the further-range quartic terms in (6), the matrix H in (8) only contains nearest-neighbor terms. In a spin-ice configuration, the coefficient of $s_i^- s_j^+$ becomes

$$H_{ij} = J + Q - \sqrt{QQ'} - QZ_iZ_j + \sqrt{QQ'}\frac{Z_iZ_{j'} + Z_jZ_{i'}}{2} \tag{19}$$

if the bond ij is on an up tetrahedron, where j', i, j, and i' are consecutive sites along a $\langle 110\rangle$ chain (cf. Fig. 12); for a down tetrahedron, $J \to J'$, $Q \leftrightarrow Q'$; the diagonal terms H_{ii} are determined by the constraint $H|Z\rangle = 0$ imposed by spin-rotation symmetry. The first three terms of (19) only renormalize J, J': unless $J' \ll J$ or Q is large compared to J, this does not affect the stability of the dynamics. The fourth term in analogous to the Q term of (9), but is halved in magnitude: this accounts for most of the reduction in the inelastic-peak frequency.

The last term depends on spins outside of the bond, so it acts as disorder on top of this renormalized BLBQ quadratic Hamiltonian. For $Q \approx Q'$, its magnitude is comparable to the renormalized Q term, so it is expected to strongly broaden the finite-frequency peak, as indeed seen in Fig. 6. To account for the remaining discrepancy in the peak frequency, we consider a simple mean-field picture, where we replace the last two terms with

$$-Z_iZ_j\left(Q - \sqrt{QQ'}\frac{\langle Z_iZ_{i'}\rangle + \langle Z_jZ_{j'}\rangle}{2}\right).$$

In nearest-neighbor spin ice at zero temperature, the correlator of two spins in this position is $\langle Z_iZ_{i'}\rangle = \langle Z_jZ_{j'}\rangle \approx 0.0883$ [37]; at $Q = Q'$, this predicts a further renormalization of

Q that brings the peak down from $8Q$ to $\approx 7.3Q$, in good quantitative agreement with Fig. 6.

A detailed account of the splitting of the renormalized $16\overline{Q}$ peak is beyond the scope of this work. However, we speculate that due to the strong but discrete [the last term of (19) can only be $\pm\sqrt{QQ'}$ or 0] disorder, the eigenmodes living on long ferromagnetic chains discussed in Sec. III A break up into short segments with equal disorder terms, leading to three peaks.

IV. DISCUSSION

To summarize, dynamical simulations of the bilinear-biquadratic Hamiltonian (2) on the breathing pyrochlore lattice with $J'/J \gtrsim 0.3$ show a dynamical structure factor made up of three components: (i) a broad inelastic peak at $16\overline{Q}$, (ii) a sharp linearly dispersing mode, and (iii) a broad, weakly dispersing continuum extending to about $4\overline{J}$. We accounted for this spectrum quantitatively in terms of small fluctuations around the spin-ice-like ground states of the nematically ordered model, similar to linear spin-wave theory for conventionally ordered magnets. In particular, feature (i) is due to collective spin precession around long *ferromagnetic* loops, while feature (ii) originates in long-wavelength fluctuations of the nematic director. We developed a similar small-fluctuation theory for the more accurate site-phonon model [13,21], which shows the same qualitative features, albeit with a renormalized dispersion relation: in particular, the position of the finite-frequency peak is renormalized down to about $7\overline{Q}$.

It is important to point out that our semiclassical approximation relies on the assumption that the low-energy sector of the interacting spin-3/2 problem are dominated by on-site dipole, rather than quadrupole or higher, moments. This is a justified assumption for spinel pyrochlores, where measurements of the exchange couplings agree on $|Q| \ll |J|$ [22,38,39]: in this limit, prior studies have found dipolar, rather than quadrupolar, low-temperature phases on a range of lattices [29–32]. An interesting but challenging direction for future work would be exploring the phase diagram and dynamics of the BLBQ model throughout the (J, Q) phase diagram.

As shown in Fig. 10, the theoretically predicted spectrum matches inelastic-neutron-scattering experiments on the nematically ordered spinel $LiGa_{0.95}In_{0.05}Cr_4O_8$ [25]. Comparing the positions of the inelastic peaks, we estimate $\overline{Q} \approx 0.35$ meV assuming the BLBQ model and $\overline{Q} \approx 0.75$ meV assuming the site-phonon model. Taking the length of the $S = 3/2$ Cr^{3+} moments into account [28], the latter corresponds to $\overline{Jb} \approx 0.22$ meV. Estimates of J and b for $LiGa_{0.95}In_{0.05}Cr_4O_8$ in the literature vary widely between $\overline{J} \approx 40$ K [22] to $\overline{J} \approx 80$ K [38,39]. For the former, our estimate yields $b \approx 0.07$, comparable to typical figures in the literature. On the other hand, the parameters proposed in Ref. [38] yield $\overline{Jb} \approx 1.0$ meV, almost an order of magnitude higher than our estimate; furthermore, their estimate of $J'/J \approx 0.04$ leads to low-temperature dynamics desribed by isolated tetrahedra, qualitatively different to the experimentally observed dynamics [25]. Earlier estimates of $J'/J \approx 0.6$ [22,39] appear more consistent with the neutron-scattering results.

The idealized BLBQ spectrum shown in, e.g., Fig. 2 differs from the experimental results in two key ways: (i) the experimental inelastic peak is far broader than the simulated $16\overline{Q}$ peak; (ii) the linearly dispersing mode is absent in the experiments. We found that the former can be explained either by finite excitation lifetime due to dynamical processes (modelled using strong Landau–Lifshitz damping α) or by static disorder in the Hamiltonian, cf. Figs. 5 and 10. The experimentally observed Gaussian shape of the peak [25], however, agrees better with the latter scenario. The additional couplings of the site-phonon model can also be regarded as strong disorder on top of the BLBQ dynamics, which indeed broaden the peak to a similar extent as seen in the experiment [cf. Figs. 10(b) and 10(c)]. We believe that the additional structure of this peak would also be washed out by either static disorder or dynamical damping. In future work, it will be interesting to extend inelastic neutron-scattering measurements to smaller values of (q, ω), where the fate of the linearly dispersing mode could be studied directly.

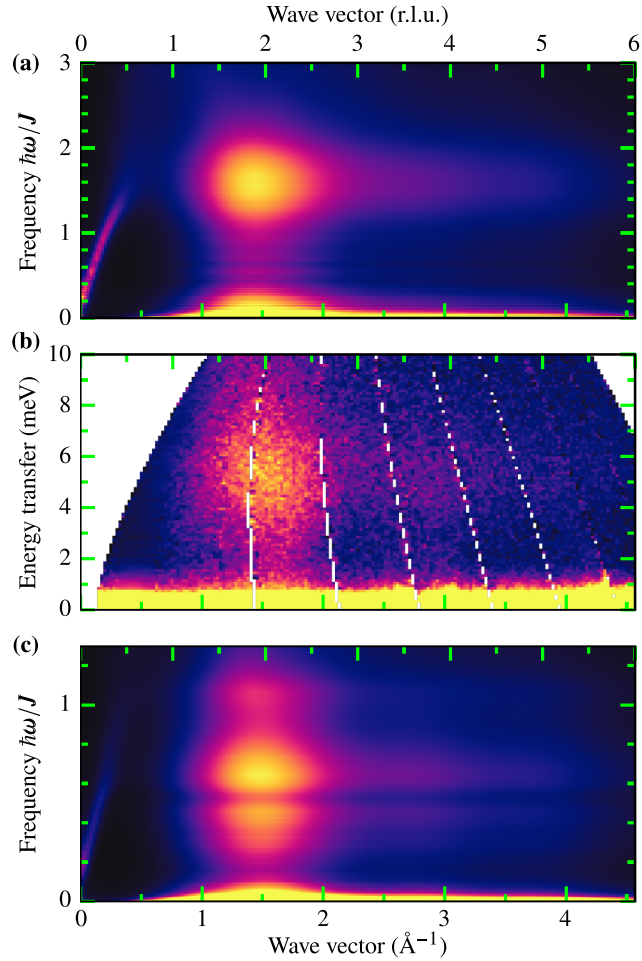

FIG. 10. (a) Simulated inelastic neutron-scattering pattern for 10% Gaussian disorder in J and Q in the BLBQ model [same parameters as Fig. 5(b)]. (b) Inelastic neutron-scattering intensity of $LiGa_{0.95}In_{0.05}Cr_4O_8$ at $T = 5.2$ K, measured with 16 meV incident neutron energy [25]. (c) Simulated inelastic neutron-scattering pattern for the site-phonon model (same parameters as Fig. 6). The data in (a) and (c) are multiplied with the Cr^{3+} magnetic form factor, and the wave vector scaled by $2\pi/a_0$ (with lattice parameter $a_0 = 8.253$ Å [26]), to aid comparison. Frequency ranges are chosen to approximately match the peak positions.

Our findings are also potentially relevant to spinel materials beyond $LiGa_{0.95}In_{0.05}Cr_4O_8$. For example, the solid solution $Zn_{2-x}Cd_xCr_2O_4$ with $x = 0.05$ shows a similar phenomenology to $LiGa_{0.95}In_{0.05}Cr_4O_8$ in both magnetic susceptibility and inelastic neutron scattering [9], raising the possibility that the nematic state is generic to chromium spinels with light disorder. The inelastic excitation energy 4 meV measured for this system [9] implies $Q_{\mathrm{BLBQ}} \approx 0.25\,\mathrm{meV}$ and $Q_{\mathrm{sp}} \approx 0.55\,\mathrm{meV}$ in the BLBQ and site-phonon models, respectively. Given the value of $J = 3.5\,\mathrm{meV}$ for the end-member $ZnCr_2O_4$ [40], the latter implies $b \approx 0.04$, consistent with the value $b \approx 0.02$ suggested by high-field magnetization measurements on $ZnCr_2O_4$ [18].

We finally note that the order-by-disorder-induced nematic phase of the classical kagome Heisenberg model [41] also exhibits sharp linearly dispersing dynamical modes on top of a partially ordered nematic background. The similarity of the ice-like ground states, as well as the dynamics, of these two systems raises the tantalising possibility of a deeper analogy between them. In future work, therefore, it will be interesting to study the long-time relaxation dynamics of the nematic order in our models. In the kagome case, this dynamics is governed by qualitatively different processes [41] from the LSWT-like precession dynamics studied in this work. The relaxation dynamics may also be affected in exotic ways by kinematic constraints, possibly analogous to the fractal dynamics recently uncovered in pyrochlore spin ice [42].

ACKNOWLEDGMENTS

We used parts of the NetKet library [43] to construct the lattices in our code. All heat maps use perceptionally uniform color maps based on Ref. [44]. Computing resources were provided by STFC Scientific Computing Department"s SCARF cluster. A.Sz. gratefully acknowledges the ISIS Neutron and Muon Source and the Oxford–ShanghaiTech collaboration for support of the Keeley–Rutherford fellowship at Wadham College, Oxford.

APPENDIX A: DETAILS OF THE DYNAMICAL SIMULATIONS

1. Monte Carlo sampling

We used Metropolis Monte Carlo with single-spin updates to draw spin configurations from the thermal ensemble of the Hamiltonian (2). In each step, the proposed spin update was constructed as

$$\vec{s}_i' = \frac{\vec{s}_i + \vec{r}_i}{|\vec{s}_i + \vec{r}_i|}, \tag{A1}$$

where each component of $\vec{r}_i$ is drawn independently from a Gaussian distribution of variance $\sigma^2 = T/(\bar{J} + 6\bar{Q})$, chosen to match thermal fluctuations under the on-site part of the LSWT Hamiltonian (9). We note that, since there are no interactions between spins on the same sublattice, the proposal–acceptance cycle can be performed in parallel for all spins of the same sublattice, allowing for efficient vectorization.

This protocol results in a temperature-independent acceptance rate at low temperatures, indicating that the thermal fluctuations around the ordered state are captured well. However, the nematically ordered moments become frozen sufficiently below the ordering temperature, resulting in rather noisy static structure factors from a single run. Therefore, to obtain the static structure factor shown in Fig. 3(a), we initialized the Monte Carlo with 256 independent spin-ice configurations obtained from a variant of the codes in Refs. [45,46].

2. Stochastic dynamics

To solve the Landau–Lifshitz dynamical equation (3), we implemented the semi-implicit integrator SIB proposed in Ref. [33]. This algorithm achieves comparable accuracy to fully symplectic solvers (such as the implicit midpoint method) at a fraction of the computational cost by exploiting the sparseness of the dynamical equation. We performed 65 536 time steps of size $\Delta t = \hbar/(16J)$ for a total simulation time $T = 4096\hbar/J$, resulting in a frequency resolution $\Delta\omega = 2\pi/T \approx 1.53 \times 10^{-3} J/\hbar$. We only saved the spin configuration after every fourth step, as this still allowed us to resolve the full dynamical spectrum.

In stochastic differential equation solvers, the noise term $\vec{b}_i$ of (3) is implemented using a noise vector $\vec{\xi}_i$, whose components should be unit Gaussian random numbers. Due to the implicitness of the solver, however, using unbounded $\vec{\xi}_i$ can lead to instabilities. Reference [33] proposes to simply apply a cutoff to Gaussian $\vec{\xi}_i$ components: we found that this results in strong numerical damping and equilibrium energies well below that obtained for the same temperature from Monte Carlo at any temperature, time step size, or value of α. By contrast, drawing $\vec{\xi}_i$ uniformly from the surface of a sphere of radius $\sqrt{3}$ (such that the standard deviation of each component is 1) resulted in energies that match the Monte Carlo results within statistical error. We believe that matching the (co)variances of the ideal Gaussian noise in any projection (not only along the Cartesian axes) is crucial for this.

For most parameter values, we ran a single dynamical simulation, as the dynamical fluctuations appear to remain self-averaging even in a frozen spin-ice background. For the parameters $J = J'$, $Q = Q' = 0.1J$, and $\alpha = 0.01$ used in Figs. 2, 3, and 7, we averaged four independent runs to improve statistics.

3. Powder averaging

To compute powder averages of q-dependent quantities, we broadened every k-point obtained from FFT with a Gaussian of standard deviation $\sigma_q = \sqrt{2\pi}/La_0$, where L is the number of cubic unit cells along each Cartesian direction (La_0 is the linear size of the simulation box) and integrated the result over bins of width Δq:

$$\begin{aligned} S_{\mathrm{powder}}(q) &= \frac{1}{4\pi q^2 \Delta q} \int_{q-\Delta q/2}^{q+\Delta q/2} dq' \sum_k S(\vec{k}) \frac{e^{-(k-q')^2/2\sigma_q^2}}{\sqrt{2\pi}\sigma_q} \\ &= \frac{1}{4\pi q^2 \Delta q} \sum_k \frac{S(\vec{k})}{2} \left[\mathrm{erf}\left(\frac{q'-k}{\sqrt{2}\sigma_q} \right) \right]_{q-\Delta q/2}^{q'=q+\Delta q/2}. \end{aligned} \tag{A2}$$

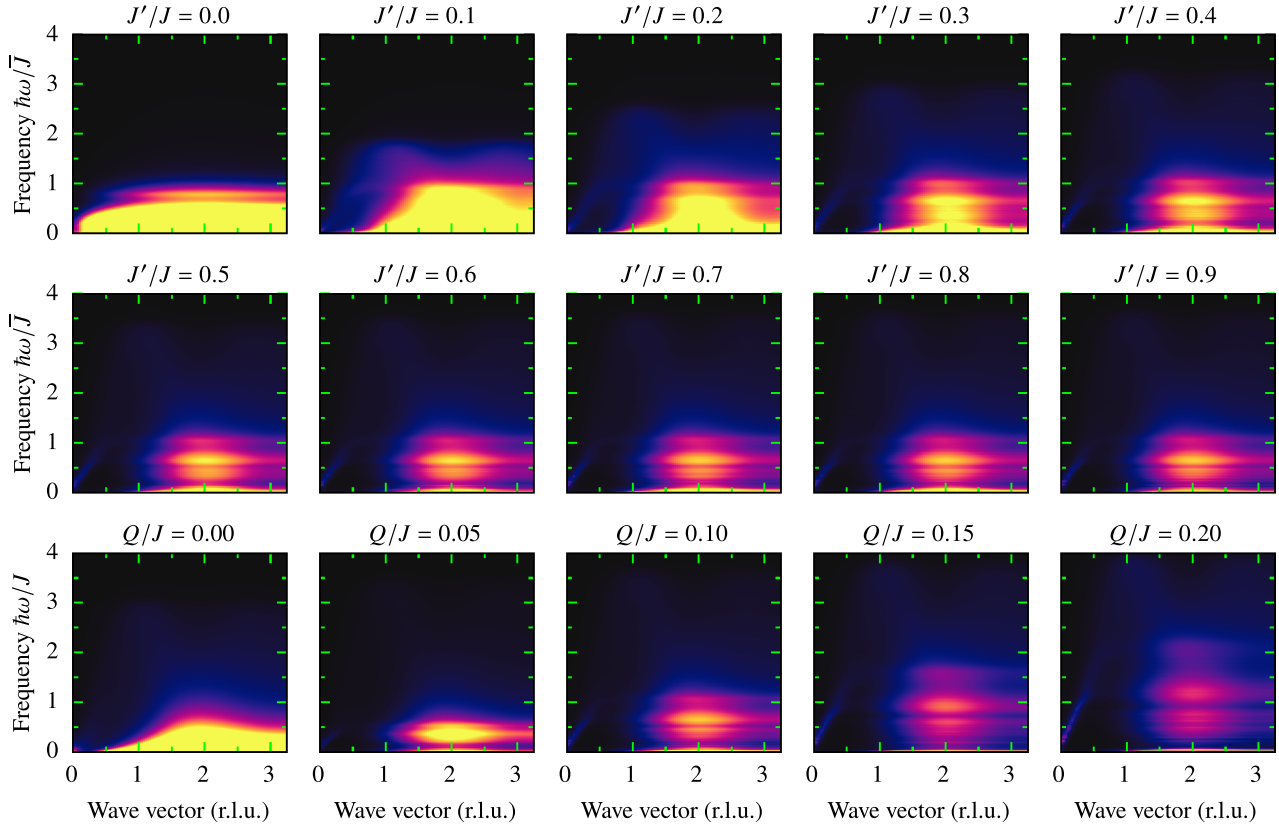

FIG. 11. Simulated powder-averaged dynamic structure factor of the site-phonon model (6) for the same parameters as used in Fig. 4 and using a cluster of 16^3 cubic unit cells.

We can think of this as spreading out the discrete k-points into three-dimensional Gaussians in reciprocal space and averaging the result over spherical shells; the denominator $4\pi q^2 \Delta q$ is the volume of such a shell. The width σ_q of the Gaussian was chosen such that the effective volume $(\sqrt{2\pi}\sigma_q)^3$ taken up by them in reciprocal space match the volume around each allowed k point, $(2\pi/La_0)^3$. Both this choice and integrating over bins of q reduce spurious fluctuations due to the discrete k points available in the finite-size system, allowing us to use the relatively narrow bin width $\Delta q = \pi/La_0$.

4. Dynamical structure factor of the site-phonon model

We performed dynamical simulations of the site-phonon model (6) for all the parameter sets used in Fig. 4. The resulting dynamical structure factors are shown in Fig. 11. Similar to the BLBQ model, we find that the finite-frequency peak and the linearly dispersing mode form clearly for all $J'/J \gtrsim 0.3$, and all quantitative features are essentially the same for all $J' \gtrsim 0.5$. The position of the main inelastic peak also appears to remain proportional to Q.

APPENDIX B: DERIVATION OF THE LSWT DYNAMICAL EQUATION

Equation (10) can be obtained by straightforwardly expanding (3) to first order in $s^{\pm}$. Here, we present an alternative derivation that makes explicit use of the quadratic Hamiltonian (8) and thus explains the presence of the matrix H in (10).

The energy-conserving dynamical term $\vec{s}_i \times \vec{B}_i$ can be obtained by applying Ehrenfest's theorem to (2) and replacing every spin operator with its expectation value [47]. Likewise, the semiclassical dynamical equation for s_i^+ is

$$\frac{ds_i^+}{dt} = \frac{d\langle \hat{s}_i^+ \rangle}{dt} = -\frac{i}{\hbar}\langle [\hat{s}_i^+, \mathcal{H}] \rangle \approx -\frac{i}{\hbar}\left\langle \left[\hat{s}_i^+, \frac{1}{2}\hat{s}_j^+ H_{jk} \hat{s}_k^- \right] \right\rangle$$
$$= -i\left\langle \hat{s}_j^+ H_{ji} \hat{s}_i^z \right\rangle \approx -\frac{i}{\hbar} Z_i H_{ij} s_j^+, \tag{B1}$$

where we also used that $\langle \hat{s}_i^z \rangle = Z_i$ to leading order.

There is no equally straightforward derivation of the dissipative term from first principles. However, the z component of $\vec{s}_i \times \vec{B}_i$ comes from the transverse components of $\vec{s}_i$, $\vec{B}_i$, so it is of second order. Therefore, the only first-order terms in $\vec{s}_i \times \vec{s}_i \times \vec{B}_i$ are due to the z component of $\vec{s}_i$ and the transverse components of $\vec{s}_i \times \vec{B}_i$:

$$(\vec{s}_i \times \vec{s}_i \times \vec{B}_i)^+ = s_i^z[-(\vec{s}_i \times \vec{B}_i)^y + i(\vec{s}_i \times \vec{B}_i)^x]$$
$$= iZ_i(\vec{s}_i \times \vec{B}_i)^+ = \tfrac{1}{\hbar} Z_i^2 H_{ij} s_j^+, \tag{B2}$$

where we substitute (B1) for $(\vec{s}_i \times \vec{B}_i)^+$. Substituting (B1) and (B2) into (3) and using that $Z_i^2 = 1$ yields (10).

APPENDIX C: MATHEMATICAL PROPERTIES OF THE LSWT EQUATIONS

We expect that H be a positive (semi)definite matrix when performing the expansion (8) near an Ising configuration that obeys the ice rules, as these minimize the Hamiltonian (2). We can show this mathematically by rewriting H as a sum of terms of the form (12) acting on individual tetrahedra. The eigenvalues of these terms are 0 (for the mode locally proportional to Z_i), $4J + 8Q$ [for the ice-rule-violating mode (1,1,1,1)], and $8Q$ (for the two modes orthogonal to both of these). That is, each term is positive semidefinite, so $\langle v|H|v\rangle \geqslant 0$ for all $|v\rangle$ as well, and zero modes must be zero modes of every term. For $Q > 0$ therefore, the only zero mode of H is that proportional to Z_i, i.e., rigid rotations of the spin-ice configuration. For $Q = 0$, every mode that respects the ice rule has zero energy, which explains the breakdown of the linear-spin-wave picture for the pure Heisenberg model.

For $\alpha = 0$, the Landau–Lifshitz dynamics (3) conserves energy. Near an energy minimum, this prevents the linear spin-wave dynamics from having any exponentially decaying or exploding modes, thus all eigenvalues of the dynamical matrix ZH must be real. To prove that this is the case, we multiply (11) with H from the left:

$$HZH|r_a\rangle = \hbar\omega_a H|r_a\rangle. \tag{C1}$$

Now, both HZH and H are Hermitian matrices, and H is positive definite [48]: this implies that the eigenvalues ω_a are all real [49]. As both matrices are also real, the eigenvectors are real, too.

We can extend these arguments to show that the eigenfrequencies of the $\alpha > 0$ dynamics have $\mathrm{Im}\,\omega \leqslant 0$, that is, they all decay. We multiply (11) from the left by $H^{1/2}$ to get

$$H^{1/2}(Z - i\alpha)H^{1/2}|\tilde{r}_a\rangle = \hbar\omega_a|\tilde{r}_a\rangle. \quad (|\tilde{r}_a\rangle \equiv H^{1/2}|r_a\rangle) \tag{C2}$$

Multiplying on the left by $\langle\tilde{r}_a|$, we find that the eigenfrequency is given by the Rayleigh quotient

$$\begin{aligned}\hbar\omega &= \frac{\langle\tilde{r}_a|H^{1/2}(Z - i\alpha)H^{1/2}|\tilde{r}_a\rangle}{\langle\tilde{r}_a|\tilde{r}_a\rangle} \\ &= \frac{\langle r_a|HZH|r_a\rangle}{\langle r_a|H|r_a\rangle} - i\alpha\frac{\langle r_a|H^2|r_a\rangle}{\langle r_a|H|r_a\rangle}.\end{aligned} \tag{C3}$$

Every matrix in the second form of (C3) is Hermitian, so $\mathrm{Im}\,\omega$ is entirely due to the second term. Furthermore, both H and H^2 are positive definite [48], so $\langle r_a|H^2|r_a\rangle/\langle r_a|H|r_a\rangle > 0$ for any $|r_a\rangle$, thus $\mathrm{Im}\,\omega_a < 0$ for all but the zero mode.

The matrix $H^{1/2}(Z - i\alpha)H^{1/2}$ in (C2) is symmetric. Complex symmetric matrices are generally not normal, so their left and right eigenvectors are different. However, taking the transpose (*not* conjugate transpose) of (C2) gives

$$\langle\tilde{r}_a^*|H^{1/2}(Z - i\alpha)H^{1/2} = \langle\tilde{r}_a^*|\hbar\omega, \tag{C4}$$

that is, $\langle\tilde{r}_a^*|$ is a left eigenvector corresponding to the same eigenvalue as $|\tilde{r}_a\rangle$. The resolvent of $H^{1/2}(Z - i\alpha)H^{1/2}$ can therefore be written as

$$[\hbar\omega - H^{1/2}(Z - i\alpha)H^{1/2}]^{-1} = \sum_a \frac{|\tilde{r}_a\rangle\langle\tilde{r}_a^*|}{\hbar(\omega - \omega_a)}, \tag{C5}$$

assuming the usual orthonormalization for left and right eigenvectors,

$$\langle\tilde{r}_a^*|\tilde{r}_b\rangle = \langle r_a^*|H|r_b\rangle = \delta_{ab}. \tag{C6}$$

Finally, multiplying (C5) on both sides by $H^{-1/2}$ gives

$$[\hbar\omega H - H(Z - i\alpha)H]^{-1} = \sum_a \frac{|r_a\rangle\langle r_a^*|}{\hbar(\omega - \omega_a)}. \tag{C7}$$

APPENDIX D: DYNAMICAL STRUCTURE FACTOR FROM LSWT

To incorporate the stochastic fluctuation terms of (3) into linear spin-wave theory, we note that the leading-order components of $\vec{s}_i \times \vec{b}_i$ and $\vec{s}_i \times \vec{s}_i \times \vec{b}_i$ are those involving the z component of $\vec{s}_i$. Therefore

$$\begin{aligned}\hbar\frac{d|s^+\rangle}{dt} &= -(iZ + \alpha)H|s^+\rangle + (iZ + \alpha)|b^+\rangle \\ -i\hbar\omega|s^+(\omega)\rangle &= -(iZ + \alpha)H|s^+(\omega)\rangle + (iZ + \alpha)|b^+(\omega)\rangle, \\ |s^+(\omega)\rangle &= [-i\hbar\omega + (iZ + \alpha)H]^{-1}(iZ + \alpha)|b^+(\omega)\rangle \\ &= -[\hbar\omega - (Z - i\alpha)H]^{-1}(Z - i\alpha)|b^+(\omega)\rangle,\end{aligned} \tag{D1}$$

where $|b^+\rangle$ is the vector of $b_i^x + ib_i^y$.

The dynamical structure factor in real space is given by the thermal average of $|s^+(\omega)\rangle\langle s^+(\omega)|$. To perform the average, we note that

$$\left\langle b_i^+(t)b_j^-(t')\right\rangle = 4D\delta_{ij}\delta(t - t') \Rightarrow \left\langle b_i^+(\omega)b_j^-(-\omega)\right\rangle = 4D\delta_{ij}, \tag{D2}$$

whence

$$\begin{aligned}\mathcal{S}(\omega) = \left\langle|s^+(\omega)\rangle\langle s^+(\omega)|\right\rangle &= [\hbar\omega - (Z - i\alpha)H]^{-1}(Z - i\alpha)4D(Z + i\alpha)[\hbar\omega - H(Z + i\alpha)]^{-1} \\ &= 4D(1 + \alpha^2)[\hbar\omega - (Z - i\alpha)H]^{-1}[\hbar\omega - H(Z + i\alpha)]^{-1} \\ &= 4D(1 + \alpha^2)[\hbar\omega - (Z - i\alpha)H]^{-1}H[\hbar\omega - (Z + i\alpha)H]^{-1}H^{-1} \\ &= \frac{2iD(1 + \alpha^2)}{\alpha}\{[\hbar\omega - (Z - i\alpha)H]^{-1} - [\hbar\omega - (Z + i\alpha)H]^{-1}\}H^{-1} \\ &= 2ik_\mathrm{B}T\hbar\{[\hbar\omega H - H(Z - i\alpha)H]^{-1} - [\hbar\omega H - H(Z + i\alpha)H]^{-1}\} \\ &= 2ik_\mathrm{B}T\sum_a\left(\frac{1}{\omega - \omega_a}\frac{|r_a\rangle\langle r_a^*|}{\langle r_a^*|H|r_a\rangle} - \frac{1}{\omega - \omega_a^*}\frac{|r_a^*\rangle\langle r_a|}{\langle r_a|H|r_a^*\rangle}\right).\end{aligned} \tag{D3}$$

In the second line, we use that Z is a diagonal matrix with ± 1 as entries. The fourth line uses the identity $(A+B)^{-1} - (A-B)^{-1} = -2(A+B)^{-1}B(A-B)^{-1}$. In the last two lines, we substitute the fluctuation–dissipation relation (4) and the spectral decomposition (C7), making the normalization (C6) explicit. The two terms in the last two lines are manifestly complex conjugate symmetric matrices, so $\mathcal{S}(\omega)$ is real and symmetric, as expected from its definition.

Equation (D3) assumes that the eigenvectors $|r_a\rangle$ satisfy the orthogonality condition (C6). For degenerate modes (such as the exact $16\overline{Q}$ modes), the eigenvectors returned by nonhermitian eigensolvers do not satisfy any such relation, so blindly applying (D3) leads to incorrect results. For the results shown in Fig. 7, we added very weak ($\Delta J/J = 10^{-6}$) bond disorder to lift all degeneracies without perceptibly changing $\mathcal{S}(\omega)$.

The q-integrated and q-resolved dynamical structure factors can be expressed from (D3) as

$$\frac{1}{N}\operatorname{tr}\mathcal{S}(\omega) = -\frac{4k_{\mathrm{B}}T}{N}\sum_a \operatorname{Im}\left(\frac{1}{\omega-\omega_a}\frac{\langle r_a^*|r_a\rangle}{\langle r_a^*|H|r_a\rangle}\right); \quad \text{(D4)}$$

$$\begin{aligned}\langle q|\mathcal{S}(\omega)|q\rangle &= -4k_{\mathrm{B}}T\sum_a \operatorname{Im}\left(\frac{1}{\omega-\omega_a}\frac{\langle q|r_a\rangle\langle r_a^*|q\rangle}{\langle r_a^*|H|r_a\rangle}\right)\\ &= -4k_{\mathrm{B}}T\sum_a \operatorname{Im}\left(\frac{1}{\omega-\omega_a}\frac{r_a(q)r_a(-q)}{\langle r_a^*|H|r_a\rangle}\right),\end{aligned} \quad \text{(D5)}$$

where $r_a(q)$ are the Fourier components of the eigenvector. Static structure factors can be obtained from these by integrating over ω and noting that

$$\mathcal{P}\int_{-\infty}^{\infty}\frac{d\omega}{2\pi}\frac{1}{\omega-\omega_a} = \frac{i}{2}\operatorname{sgn}(\operatorname{Im}\omega_a) = -i/2$$

for every ω_a in the lower half plane. In particular, the mean square transverse fluctuation of each spin is given by

$$\langle s_i^+ s_i^-\rangle = \frac{1}{N}\int_{-\infty}^{\infty}\frac{d\omega}{2\pi}\operatorname{tr}\mathcal{S}(\omega) = \frac{2k_{\mathrm{B}}T}{N}\sum_{a\neq 0}\operatorname{Re}\frac{\langle r_a^*|r_a\rangle}{\langle r_a^*|H|r_a\rangle}; \quad \text{(D6)}$$

the zero mode must be excluded as it does not correspond to transverse fluctuations around a nematic state but rotating its director.

We finally note that in the limit $\alpha \to 0^+$, $1/(\omega-\omega_a) \to \mathcal{P}1/(\omega-\omega_{0a}) - i\pi\delta(\omega-\omega_{0a})$, so (D3) becomes

$$\mathcal{S}(\omega) = 2k_{\mathrm{B}}T\sum_a \frac{|r_a\rangle\langle r_a|}{\langle r_a|H|r_a\rangle}2\pi\delta(\omega-\omega_{0a}). \quad \text{(D7)}$$

That is, each eigenmode of ZH gives rise to a sharp peak in the structure factor, with a spatial structure matching the eigenvector $|r\rangle$ and intensity normalized by the energy cost $\langle r|H|r\rangle$ of exciting the mode.

APPENDIX E: QUADRATIC EXPANSION OF THE SITE-PHONON HAMILTONIAN

Substituting (7) into $\vec{s}_i\cdot\vec{s}_j$ and expanding to second order in $s^\pm$ yields

$$\vec{s}_i\cdot\vec{s}_j \simeq Z_iZ_j + \tfrac{1}{2}\underbrace{[s_i^+s_j^- + s_j^+s_i^- - Z_iZ_j(s_i^+s_i^- + s_j^+s_j^-)]}_{b_{ij}}. \quad \text{(E1)}$$

Since this has no linear term in $s^\pm$, all quadratic terms in the expansion of any $(\vec{s}_i\cdot\vec{s}_j)(\vec{s}_k\cdot\vec{s}_l)$ contain the zeroth-order term of one $\vec{s}\cdot\vec{s}$ and the quadratic term of the other. In particular, the quartic term of the site-phonon Hamiltonian (6) becomes

$$\begin{aligned}H_{\mathrm{sp}}^Q &\simeq -\frac{1}{2}\sum_i\sum_{j,k\sim i}\sqrt{Q_{ij}Q_{ik}}(\hat{e}_{ij}\cdot\hat{e}_{ik})\frac{Z_iZ_jb_{ik} + Z_iZ_kb_{ij}}{2}\\ &= -\frac{1}{2}\sum_i\sum_{j,k\sim i}\sqrt{Q_{ij}Q_{ik}}(\hat{e}_{ij}\cdot\hat{e}_{ik})Z_iZ_kb_{ij}\end{aligned} \quad \text{(E2)}$$

up to an overall constant. Since the only quadratic terms come from expanding nearest-neighbor $\vec{s}_i\cdot\vec{s}_j$, Eq. (E2) is still nearest-neighbor. The expanded BLBQ Hamiltonian (9) can be recovered from (E2) by keeping the $j=k$ terms only.

Let us now consider the b_{ij} terms in (E2) where i appears in the outer sum. For convenience, we assume that the bond ij is on an up tetrahedron; for a down tetrahedron, $Q \leftrightarrow Q'$. Writing out the sum over k explicitly, we get

$$\begin{aligned}&\frac{b_{ij}}{2}\left[-Q\left(Z_iZ_j + \frac{1}{2}Z_iZ_k + \frac{1}{2}Z_iZ_l\right)\right.\\ &\qquad\left. + \sqrt{QQ'}\left(Z_iZ_{j'} + \frac{1}{2}Z_iZ_{k'} + \frac{1}{2}Z_iZ_{l'}\right)\right] \quad \text{(E3)}\\ &= \frac{b_{ij}}{2}\left[-\frac{Q}{2}Z_iZ_j + \frac{Q}{2} + \frac{\sqrt{QQ'}}{2}Z_iZ_{j'} - \frac{\sqrt{QQ'}}{2}\right], \quad \text{(E4)}\end{aligned}$$

where the site labels are as shown in Fig. 12. In (E4), we also assume that the Z_i form a spin-ice configuration such that $Z_j + Z_k + Z_l = Z_{j'} + Z_{k'} + Z_{l'} = -Z_i$. After including the terms where j appears in the outer sum, we get the complete b_{ij} term:

$$\frac{b_{ij}}{2}\left[(Q-\sqrt{QQ'}) - QZ_iZ_j + \sqrt{QQ'}\frac{Z_iZ_{j'} + Z_jZ_{i'}}{2}\right]. \quad \text{(E5)}$$

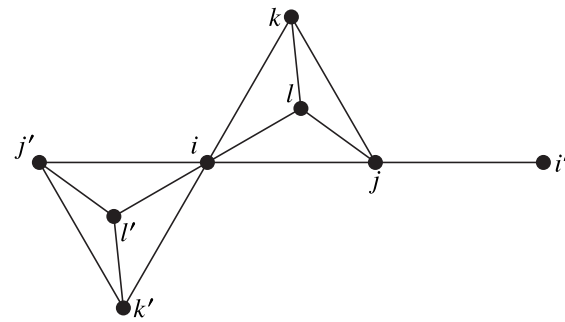

FIG. 12. Layout of site labels used in (E3).

[1] C. Castelnovo, R. Moessner, and S. L. Sondhi, Spin ice, fractionalization, and topological order, Annu. Rev. Condens. Matter Phys. **3**, 35 (2012).

[2] L. Balents, Spin liquids in frustrated magnets, Nature (London) **464**, 199 (2010).

[3] L. Savary and L. Balents, Quantum spin liquids: a review, Rep. Prog. Phys. **80**, 016502 (2017).

[4] L. Clark and A. H. Abdeldaim, Quantum spin liquids from a materials perspective, Annu. Rev. Mater. Res. **51**, 495 (2021).

[5] S. Ji, S.-H. Lee, C. Broholm, T. Y. Koo, W. Ratcliff, S.-W. Cheong, and P. Zschack, Spin-lattice order in frustrated $ZnCr_2O_4$, Phys. Rev. Lett. **103**, 037201 (2009).

[6] O. Tchernyshyov, R. Moessner, and S. L. Sondhi, Spin-Peierls phases in pyrochlore antiferromagnets, Phys. Rev. B **66**, 064403 (2002).

[7] P. H. Conlon and J. T. Chalker, Absent pinch points and emergent clusters: Further neighbor interactions in the pyrochlore Heisenberg antiferromagnet, Phys. Rev. B **81**, 224413 (2010).

[8] A. B. Sushkov, O. Tchernyshyov, W. Ratcliff II, S. W. Cheong, and H. D. Drew, Probing spin correlations with phonons in the strongly frustrated magnet $ZnCr_2O_4$, Phys. Rev. Lett. **94**, 137202 (2005).

[9] W. Ratcliff II, S.-H. Lee, C. Broholm, S.-W. Cheong, and Q. Huang, Freezing of spin correlated nanoclusters in a geometrically frustrated magnet, Phys. Rev. B **65**, 220406(R) (2002).

[10] K. Penc, N. Shannon, and H. Shiba, Half-magnetization plateau stabilized by structural distortion in the antiferromagnetic Heisenberg model on a pyrochlore lattice, Phys. Rev. Lett. **93**, 197203 (2004).

[11] H. Shinaoka, Y. Tomita, and Y. Motome, Effect of magnetoelastic coupling on spin-glass behavior in Heisenberg pyrochlore antiferromagnets with bond disorder, Phys. Rev. B **90**, 165119 (2014).

[12] A. Miyata, H. Ueda, Y. Ueda, H. Sawabe, and S. Takeyama, Magnetic phases of a highly frustrated magnet, $ZnCr_2O_4$, up to an ultrahigh magnetic field of 600 T, Phys. Rev. Lett. **107**, 207203 (2011).

[13] D. L. Bergman, R. Shindou, G. A. Fiete, and L. Balents, Models of degeneracy breaking in pyrochlore antiferromagnets, Phys. Rev. B **74**, 134409 (2006).

[14] R. Wawrzyńczak, Y. Tanaka, M. Yoshida, Y. Okamoto, P. Manuel, N. Casati, Z. Hiroi, M. Takigawa, and G. J. Nilsen, Classical spin nematic transition in $LiGa_{0.95}In_{0.05}Cr_4O_8$, Phys. Rev. Lett. **119**, 087201 (2017).

[15] C. Kittel, Model of exchange-inversion magnetization, Phys. Rev. **120**, 335 (1960).

[16] R. Moessner and J. T. Chalker, Properties of a classical spin liquid: The Heisenberg pyrochlore antiferromagnet, Phys. Rev. Lett. **80**, 2929 (1998).

[17] P. W. Anderson, Ordering and antiferromagnetism in ferrites, Phys. Rev. **102**, 1008 (1956).

[18] A. Miyata, H. Ueda, Y. Ueda, Y. Motome, N. Shannon, K. Penc, and S. Takeyama, Magnetic phases of $ZnCr_2O_4$ revealed by magneto-optical studies under ultra-high magnetic fields of up to 600 T, J. Phys. Soc. Jpn. **81**, 114701 (2012).

[19] A. Miyata, H. Ueda, and S. Takeyama, Canted 2:1:1 magnetic supersolid phase in a frustrated magnet $MgCr_2O_4$ as a small limit of the biquadratic spin interaction, J. Phys. Soc. Jpn. **83**, 063702 (2014).

[20] D. Nakamura, A. Miyata, Y. Aida, H. Ueda, and S. Takeyama, Optical detection of magnetic orders in $HgCr_2O_4$ frustrated spin magnet under pulsed high magnetic fields, J. Phys. Soc. Jpn. **83**, 113703 (2014).

[21] K. Aoyama and H. Kawamura, Spin ordering induced by lattice distortions in classical Heisenberg antiferromagnets on the breathing pyrochlore lattice, Phys. Rev. B **99**, 144406 (2019).

[22] Y. Okamoto, G. J. Nilsen, J. P. Attfield, and Z. Hiroi, Breathing pyrochlore lattice realized in *A*-site ordered spinel oxides $LiGaCr_4O_8$ and $LiInCr_4O_8$, Phys. Rev. Lett. **110**, 097203 (2013).

[23] G. J. Nilsen, Y. Okamoto, T. Masuda, J. Rodriguez-Carvajal, H. Mutka, T. Hansen, and Z. Hiroi, Complex magnetostructural order in the frustrated spinel $LiInCr_4O_8$, Phys. Rev. B **91**, 174435 (2015).

[24] R. Saha, F. Fauth, M. Avdeev, P. Kayser, B. J. Kennedy, and A. Sundaresan, Magnetodielectric effects in *a*-site cation-ordered chromate spinels $LiMCr_4O_8$ (M = Ga and In), Phys. Rev. B **94**, 064420 (2016).

[25] Y. Tanaka, R. Wawrzyńczak, M. D. Le, T. Guidi, Y. Okamoto, T. Yajima, Z. Hiroi, M. Takigawa, and G. J. Nilsen, Inelastic neutron scattering study of the spin dynamics in the breathing pyrochlore system $LiGa_{0.95}In_{0.05}Cr_4O_8$, J. Phys. Soc. Jpn. **87**, 073710 (2018).

[26] Y. Okamoto, G. J. Nilsen, T. Nakazono, and Z. Hiroi, Magnetic phase diagram of the breathing pyrochlore antiferromagnet $LiGa_{1-x}In_xCr_4O_8$, J. Phys. Soc. Jpn. **84**, 043707 (2015).

[27] R. G. Melko and M. J. Gingras, Monte Carlo studies of the dipolar spin ice model, J. Phys.: Condens. Matter **16**, R1277 (2004).

[28] If $S \neq 1$, our dynamical results remain applicable if J, Q are replaced with JS, QS^3. The powers of S are determined by the number of spin operators in the effective Landau–Lifshitz field $\vec{B}_i = -\partial\mathcal{H}/\partial\vec{s}_i$.

[29] A. Smerald and N. Shannon, Theory of spin excitations in a quantum spin-nematic state, Phys. Rev. B **88**, 184430 (2013).

[30] R. A. Muniz, Y. Kato, and C. D. Batista, Generalized spin-wave theory: Application to the bilinear-biquadratic model, Prog. Theor. Exp. Phys. **2014**, 083I01 (2014).

[31] A. Smerald, H. T. Ueda, and N. Shannon, Theory of inelastic neutron scattering in a field-induced spin-nematic state, Phys. Rev. B **91**, 174402 (2015).

[32] C. Luo, T. Datta, and D.-X. Yao, Spin and quadrupolar orders in the spin-1 bilinear-biquadratic model for iron-based superconductors, Phys. Rev. B **93**, 235148 (2016).

[33] J. H. Mentink, M. V. Tretyakov, A. Fasolino, M. I. Katsnelson, and T. Rasing, Stable and fast semi-implicit integration of the stochastic Landau-Lifshitz equation, J. Phys.: Condens. Matter **22**, 176001 (2010).

[34] M. Lakshmanan, The fascinating world of the Landau-Lifshitz-Gilbert equation: an overview, Philos. Trans. R. Soc. London A **369**, 1280 (2011).

[35] C. L. Henley, Power-law spin correlations in pyrochlore antiferromagnets, Phys. Rev. B **71**, 014424 (2005).

[36] Strictly speaking, we get four bands corresponding to the four fcc sublattices of the pyrochlore lattice. However, the eigenvector of the lowest band is $(1, 1, 1, 1) + O(k^2)$, so we can treat the exact low-energy eigenvectors as plane waves to leading order. The higher-order corrections are responsible for the dispersive features at other Γ points seen in Fig. 3(b).

[37] A. Szabó, Real-space correlation functions of nearest-neighbour spin ice, 10.5281/zenodo.8186611.

[38] M. Gen, A. Ikeda, K. Aoyama, H. O. Jeschke, Y. Ishii, H. Ishikawa, T. Yajima, Y. Okamoto, D. Nakamura, S. Takeyama, K. Kindo, Y. H. Matsuda, and Y. Kohama, Signatures of a magnetic superstructure phase induced by ultrahigh magnetic fields in a breathing pyrochlore antiferromagnet, Proc. Natl. Acad. Sci. USA **120**, e2302756120 (2023).

[39] P. Ghosh, Y. Iqbal, T. Müller, R. T. Ponnaganti, R. Thomale, R. Narayanan, J. Reuther, M. J. P. Gingras, and H. O. Jeschke, Breathing chromium spinels: a showcase for a variety of pyrochlore heisenberg hamiltonians, npj Quantum Mater. **4**, 63 (2019).

[40] H. Martinho, N. O. Moreno, J. A. Sanjurjo, C. Rettori, A. J. García-Adeva, D. L. Huber, S. B. Oseroff, W. Ratcliff, S.-W. Cheong, P. G. Pagliuso, J. L. Sarrao, and G. B. Martins, Magnetic properties of the frustrated antiferromagnetic spinel $ZnCr_2O_4$ and the spin-glass $Zn_{1-x}Cd_xCr_2O_4 (x = 0.05, 0.10)$, Phys. Rev. B **64**, 024408 (2001).

[41] M. Taillefumier, J. Robert, C. L. Henley, R. Moessner, and B. Canals, Semiclassical spin dynamics of the antiferromagnetic Heisenberg model on the kagome lattice, Phys. Rev. B **90**, 064419 (2014).

[42] J. N. Hallén, S. A. Grigera, D. A. Tennant, C. Castelnovo, and R. Moessner, Dynamical fractal and anomalous noise in a clean magnetic crystal, Science **378**, 1218 (2022).

[43] F. Vicentini, D. Hofmann, A. Szabó, D. Wu, C. Roth, C. Giuliani, G. Pescia, J. Nys, V. Vargas-Calderón, N. Astrakhantsev, and G. Carleo, NetKet 3: Machine learning toolbox for many-body quantum systems, SciPost Phys. Codebases **7**, (2022).

[44] P. Kovesi, Good colour maps: How to design them, arXiv:1509.03700.

[45] A. Szabó, Monte Carlo simulations of pyrochlore iridates, https://github.com/attila-i-szabo/Ho2Ir2O7/releases/tag/v1.0.

[46] M. J. Pearce, K. Götze, A. Szabó, T. S. Sikkenk, M. R. Lees, A. T. Boothroyd, D. Prabhakaran, C. Castelnovo, and P. A. Goddard, Magnetic monopole density and antiferromagnetic domain control in spin-ice iridates, Nat. Commun. **13**, 444 (2022).

[47] A. Szabó and C. Castelnovo, Seeing beyond the light: Vison and photon electrodynamics in quantum spin ice, Phys. Rev. B **100**, 014417 (2019).

[48] The zero mode of H could cause problems. However, it is obviously a zero mode of ZH too, so we could remove it from the basis and work with a positive definite H. Note also that this (semi)definiteness relies on the reference configuration being a minimum of $\mathcal{H}$: around a generic Ising configuration, the dynamical matrix will have complex eigenvalues corresponding to instabilities near ice-rule-violating tetrahedra.

[49] B. N. Parlett, *The Symmetric Eigenvalue Problem* (Society for Industrial and Applied Mathematics, 1998).